

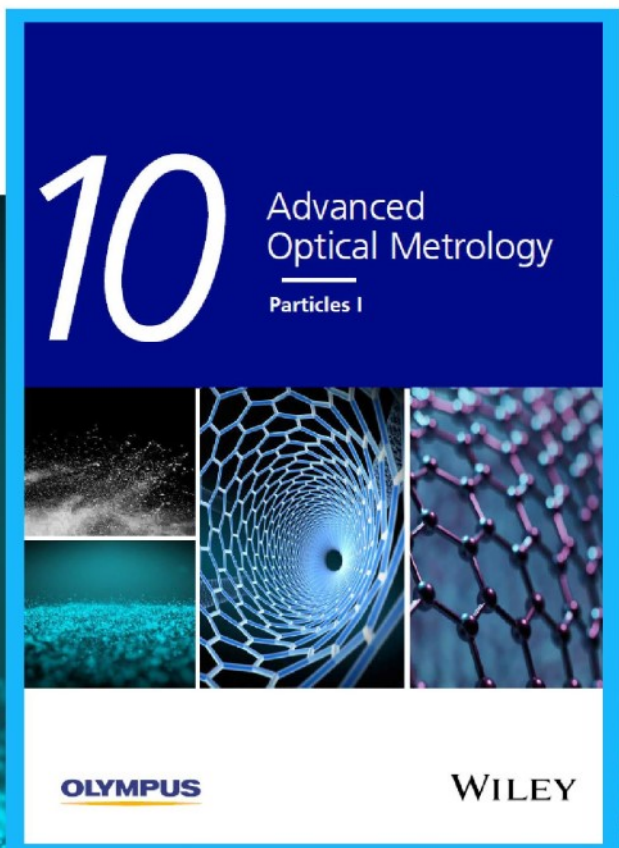


Particles I

Access the latest eBook →

Particles: Unique Properties,
Uncountable Applications

**Read the latest eBook and
better your knowledge with
highlights from the recent
studies on the design and
characterization of micro-
and nanoparticles for
different application areas.**



Access Now

This eBook is sponsored by

OLYMPUS

WILEY

Structural Dynamics and Tunability for Colloidal Tin Halide Perovskite Nanostructures

Kushagra Gahlot, Sytze de Graaf, Herman Duim, Georgian Nedelcu, Razieh M. Koushki, Majid Ahmadi, Dnyaneshwar Gavhane, Alessia Lasorsa, Oreste De Luca, Petra Rudolf, Patrick C. A. van der Wel, Maria A. Loi, Bart J. Kooi, Giuseppe Portale, Joaquín Calbo, and Loredana Protesescu*

Lead halide perovskite nanocrystals are highly attractive for next-generation optoelectronics because they are easy to synthesize and offer great compositional and morphological tunability. However, the replacement of lead by tin for sustainability reasons is hampered by the unstable nature of Sn^{2+} oxidation state and by an insufficient understanding of the chemical processes involved in the synthesis. Here, an optimized synthetic route is demonstrated to obtain stable, tunable, and monodisperse CsSnI_3 nanocrystals, exhibiting well-defined excitonic peaks. Similar to lead halide perovskites, these nanocrystals are prepared by combining a precursor mixture of SnI_2 , oleylamine, and oleic acid, with a Cs-oleate precursor. Among the products, nanocrystals with 10 nm lateral size in the γ -orthorhombic phase prove to be the most stable. To achieve such stability, an excess of precursor SnI_2 as well as substoichiometric Sn:ligand ratios are key. Structural, compositional, and optical investigations complemented by first-principle density functional theory calculations confirm that nanocrystal nucleation and growth follow the formation of $(\text{R-NH}_3^+)_2\text{SnI}_4$ nanosheets, with $\text{R} = \text{C}_{18}\text{H}_{35}$. Under specific synthetic conditions, stable mixtures of 3D nanocrystals CsSnI_3 and 2D nanosheets (Ruddlesden–Popper $(\text{R-NH}_3^+)_2\text{Cs}_{n-1}\text{Sn}_n\text{I}_{3n+1}$ with $n > 1$) are obtained. These results set a path to exploiting the high potential of Sn halide perovskite nanocrystals for opto-electronic applications.

1. Introduction

Metal halide perovskite nanocrystals (NCs) with lead (Pb^{2+})^[1,2] as the divalent cation, are attractive systems for applications such as photovoltaics,^[3] light emission and detection,^[4,5] lasing,^[5] and water-splitting^[6] because of their size and morphology tunability, enhanced optical properties, and chemical stability. However, when lead is replaced by less toxic^[7,8] divalent metals, such as Sn^{2+} ,^[9,10–12,13] the resulting NCs are reported to suffer from poor chemical stability, lack of tunability, and less appealing optical properties. In contrast, bulk^[14,15,16] and thin films^[17] of Sn halide perovskites have evolved strongly since they were first explored more than fifty years ago.^[18] Their improved performance in photovoltaics results from successful stabilization of the active layer by using additives (such as SnF_2 ^[19] and ionic liquids^[20]) or by switching from 3D structures to 2D hybrid perovskites (Dion–Jacobson^[8,21] and Ruddlesden–Popper (RP)^[22,23]). The stability reinforcements obtained in bulk materials cannot be simply translated

to the nanoscale because of two main challenges: i) the high surface-to-volume ratio for NCs below $L_1 = 10$ nm (where L_1 is the smallest lateral size of the cuboid), which causes Sn^{2+} to Sn^{4+} oxidation for a large percentage of the metal ions, and ii) the existence of polymorphs with optical bandgaps differing by as much as 1.25 eV^[15,16] (i.e., the highly conductive black cubic phase ($Pm3m$) with strong photoluminescence (PL), the γ -orthorhombic phase ($Pnma$) and the nonconductive yellow orthorhombic phase ($Pnma$)).^[15,16,24]

Reports on synthesis and surface chemistry of CsSnX_3 NCs are scarce.^[9,10–12] Those few existing cite Sn^{2+} and I^- precursors such as SnX_2 ,^[9,10] ($\text{X} = \text{Cl}^-, \text{Br}^-, \text{I}^-$), Sn-oxalates,^[11] trimethylsilyl iodide,^[10,25] and common ligands (oleylamine (OLA), oleic acid (OA), octylphosphine) used in a standard hot-injection method. However, the overall stability and performance of the obtained NCs are clearly behind those of the Pb-based analogues. While the more oxidative character of Sn^{2+} is widely recognized, the kinetic parameters involved in the nucleation and growth of the nanostructures are not yet well determined. Therefore, it is

K. Gahlot, S. de Graaf, H. Duim, G. Nedelcu, R. M. Koushki, M. Ahmadi, D. Gavhane, A. Lasorsa, O. De Luca, P. Rudolf, P. C. A. van der Wel, M. A. Loi, B. J. Kooi, G. Portale, L. Protesescu
Zernike Institute for Advanced Materials
University of Groningen
Nijenborgh 4, Groningen 9747AG, The Netherlands
E-mail: l.protesescu@rug.nl

J. Calbo
Institute of Molecular Science
Universitat de València
c/Catedrático José Beltrán, 2, Paterna 46980, Spain

 The ORCID identification number(s) for the author(s) of this article can be found under <https://doi.org/10.1002/adma.202201353>.

© 2022 The Authors. Advanced Materials published by Wiley-VCH GmbH. This is an open access article under the terms of the Creative Commons Attribution License, which permits use, distribution and reproduction in any medium, provided the original work is properly cited.

DOI: 10.1002/adma.202201353

imperative to rationalize the synthetic steps and identify intermediate compounds when moving to other metals than lead in halide perovskites. The chemical composition and stability of the Sn halide perovskite nanostructures will evince enhanced sensitivity to chemical strategies considering the ionic character of the tin halide perovskites, the solubility differences and electron affinity changes from one divalent cation to another.

Herein, we present a general route to obtain tunable and stable CsSnI₃ perovskite NCs alone or coexisting with 2D hybrid-perovskite RP nanostructures ((R-NH₃⁺)₂Cs_{n-1}Sn_nI_{3n+1}, R = C₁₈H₃₅) depending on the main synthetic parameters. The discussion is supported by density functional theory (DFT) calculations for the electronic parameters of the CsSnI₃ and (R-NH₃⁺)₂Cs_{n-1}Sn_nI_{3n+1} structures and their stability. Their morphologies and compositions are clarified using X-ray diffraction and scattering techniques, scanning transmission electron microscopy (STEM), solid-state NMR (ssNMR) and elemental analysis, complemented by optical methods. Moreover, we demonstrate the composition and structural dynamics starting from (R-NH₃⁺)₂SnI₄ (*n* = 1) to 3D CsSnI₃ NCs or to 2D (R-NH₃⁺)₂Cs_{n-1}Sn_nI_{3n+1} (*n* > 1) nanosheets.

2. Results and Discussion

Our chemical design follows the one previously proposed by reports on the synthesis of lead halide perovskite NCs.^[1,26] A supersaturated solution of a SnI₂/OLA/OA mixture in octadecene is exposed to high temperatures (*T* > 160 °C), and immediately, the Cs-oleate precursor is injected. The NCs are allowed to grow for a few seconds to one minute to reach their thermodynamically more stable structure and morphology. Using this methodology, we successfully synthesized cuboid structures (with the larger lateral dimension $L_1 = L_2 + 2$ nm, Figure 1b) with a black γ -orthorhombic *Pnma* phase (abbreviated to B- γ ; Figure 1). The L_1 of these cuboids is 10 nm as measured by STEM-high-angle annular dark-field (STEM-HAADF) (Figure 1d–f, Figure S1, Supporting Information) and confirmed by solution small-angle X-ray scattering (SAXS) analysis (Figure 2a, green circles, Figure S2, Supporting Information).

The main deviations from the lead halide perovskite NCs procedures are a much higher concentration of the SnI₂ and a substoichiometric ligands supply. These changes were undertaken because of the slightly higher hardness of the Sn²⁺ acid (according to HSAB theory),^[27] implying that the latter displays a higher reactivity with hard bases (such as R-COO⁻ or R-NH₂). The increased Lewis acid character^[28] of Sn²⁺ promotes the formation of complexes with the added bases in the crude mixture.^[29] In general, the solubility of the Sn²⁺ halide salts in various polar solvents were already reported to be higher than that of Pb²⁺ ones.^[30]

Thus, to preserve the stability of the obtained CsSnI₃ NCs and prevent their reversible reaction that yields mainly CsI, SnI₂, and oleates as byproducts, the concentration of SnI₂ was set higher than 0.1 M while maintaining a precise ratio of Sn:OLA:OA (1:1:1). Smaller NCs (lateral size $L_1 = 6$ nm) can be obtained via a similar procedure and by applying size selection on the final crude mixture (Figure 2a, blue circles; Figure S3a–c, Supporting Information for the procedure). NCs with $L_1 = 6$ nm

could not be stabilized for more than an hour. Moreover, NCs with $L_1 < 6$ nm were not observed in any synthetic procedure explored here.

To investigate the reason for their instability, we simulated CsSnI₃ NCs in a cluster approximation by replicating the unit cell of black CsSnI₃ polymorphs in the three space directions and with charge neutrality conditions (see Section SIV, Supporting Information for computational details). After geometry relaxation of a medium-size CsSnI₃ NC of 3.5 nm at the PBEsol level, the minimum-energy structure indicates that α , β and γ -CsSnI₃ NCs evolve to a disordered disposition with octahedral tilting and rotations resembling the γ -orthorhombic phase. In fact, relative stability calculations demonstrate that the optimized NC geometry coming from γ phase is the most stable structure (Figure S4, Supporting Information), thus supporting the experimental evidence. Otherwise, DFT calculations point to a progressive stabilization of the system upon increasing the NC size, suggesting a stability plateau around 6–8 nm (Figures S5 and S6). This result is in good accordance with the smallest NC population achieved experimentally ($L_1 = 6$ nm) and could explain the limited range of sizes obtainable for CsSnI₃ NCs.

The stoichiometry of the NCs was analyzed by using STEM combined with energy-dispersive X-ray analysis (EDX in so-called spectrum-imaging mode, Figure 1g–j), X-ray photoelectron spectroscopy (XPS), and X-ray fluorescence (XRF). We observed an excess of Sn and I in the CsSnI₃ NCs, which increases with decreasing the NC size (Tables S1a–c, Figure S7, Supporting Information). We conclude that the surface of the NCs is terminated predominantly with Sn-oleate and oleylammonium iodide ((R-NH₃⁺)I⁻). Moreover, we noted that, while taking great care to avoid contact with air when preparing the samples for XPS measurements, the smaller NCs ($L_1 = 6$ nm) are prone to faster surface oxidation compared to the larger ones ($L_1 = 10$ nm) since a ratio of Sn²⁺:Sn⁴⁺ = 4:1 was found for the smaller NCs (Figure S7, Supporting Information).

To further understand the mechanistic processes involved during the formation of the CsSnI₃ NCs, we varied the Cs:Sn ratio from 1:6 to 3:1 and calculated the possibility of CsSnI₃ NCs to be formed while taking into account other byproducts (Figure 3a). Then we compared those results with our experimental data (Figure 3b,c). This detailed study of the influence of the Cs:Sn ratio already reveals an important outcome: theoretically, when Sn²⁺ is in high excess in the precursor mixture (Cs:Sn = 1:6, 1:3 or 1:2), no extra Cs⁺ is obtained together with the CsSnI₃ NCs if we consider a total transformation. In this case, only Sn²⁺ and I⁻ are left in the final reaction mixture together with the remaining ligands (Figure 3b, Cs:Sn = 1:3 case). The experiments indeed confirmed that using SnI₂ in high excess always yields stable CsSnI₃ NCs with a PL peak at 714 nm (1.76 eV) (Figure 3c). Furthermore, the elemental analysis shows that for CsSnI₃ NCs [Cs]:[Sn] < 1, thus confirming the theoretical assumptions, and that extra Sn²⁺ and I⁻ are needed to stabilize the particles.

In addition, one can also expect the formation of the (R-NH₃⁺)₂SnI₄ from the remaining byproducts. To verify if those structures are stable while using the R-NH₃⁺ as a monovalent cation, we performed control reactions where we excluded the injections of Cs-oleate while maintaining the rest of the reaction parameters precisely constant. We indeed obtained stable

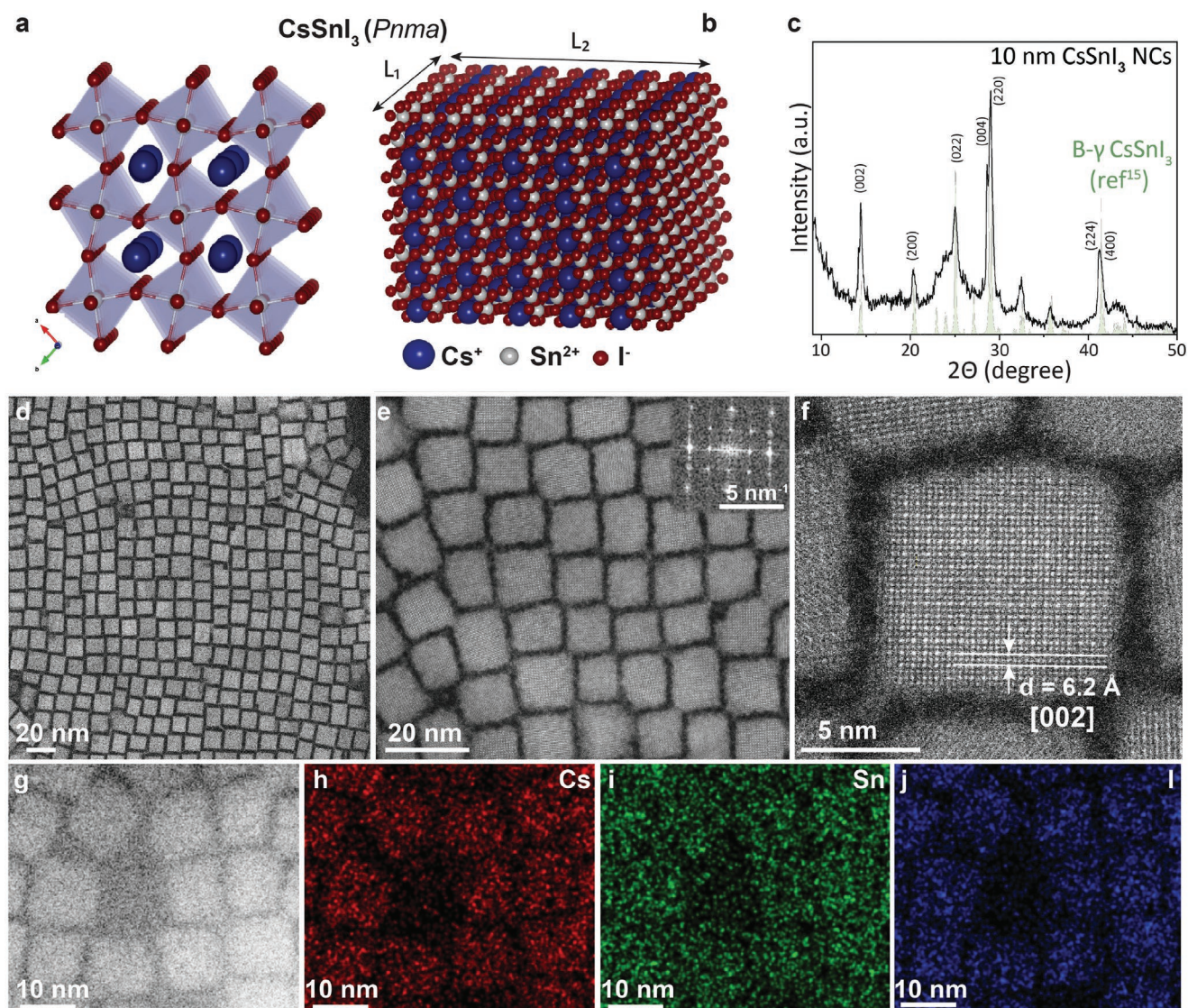


Figure 1. a, b) Schematics of the crystal structure (a) and cuboid nanocrystals (b) of the B- γ -CsSnI₃ phase (*Pnma*). c) Powder X-ray diffraction pattern of L₁ = 10 nm B- γ -CsSnI₃ nanocrystals (black) with the reference^[15] for the B- γ -CsSnI₃ (green). d, e) STEM-HAADF images of 10 nm B- γ -CsSnI₃ nanocrystals with fast Fourier transform (FFT) pattern in the inset. f) High-resolution STEM-HAADF image with a lattice distance, $d = 6.2$ Å corresponding to the [002] plane. h–j) STEM-EDX elemental mapping for the image area depicted in g) with the distribution of Cs (red) (h), Sn (green) (i), and I (blue) (j).

(R-NH₃⁺)₂SnI₄ with a PL peak at 635 nm (1.95 eV, Figure S8, Supporting Information) and showing a clear ssNMR signature for ¹¹⁹Sn at −180.5 ppm (Figure S9, Supporting Information). The SAXS analysis (Figure 2b) and the low-angle XRD measurements confirm the presence of the 2D nanosheets (Figure S10, Supporting Information). This control experiment is the first indication that the formation of the 3D CsSnI₃ NCs starts from a (R-NH₃⁺)₂SnI₄ ensemble.

After finding that 2D RP Sn-halide perovskite structures can be obtained when the precursor mixture contains a high excess of Sn²⁺, we analyzed the other extreme of Cs:Sn ratios, where Cs is in excess. In this case, in addition to the CsSnI₃ NCs, we also expect to obtain Cs-oleate and other byproducts, such as Sn-oleate and R-NH₃⁺I[−] (if we consider that the transformation of SnI₂ into CsSnI₃ is not 100% favorable). With that in mind, we hypothesized that the formation of the 2D perovskite

structures (R-NH₃⁺)₂Cs_{*n*−1}Sn_{*n*}I_{3*n*+1} with $n > 1$ is plausible. At the intermediate concentration (Cs:Sn = 1:1.5 and 1:2), an equilibrium between the 3D and 2D perovskites is expected, and can be also reproduced experimentally as evident from two emitting populations in the PL spectra (Figure 3b,c). For the specific case, when the ratio of Cs:Sn = 1:1, our experimental results (Figure 3b,c) reveal a broad emission obtained at 812 nm (1.53 eV), with final products not stable enough for further characterization.

Conjointly, Cs:Sn = 1:2 and Sn:OLA:OA = 1:2:2 can result in the formation of both 3D CsSnI₃ NCs (L₁ = 10 nm cuboids NCs) and 2D (R-NH₃⁺)₂Cs_{*n*−1}Sn_{*n*}I_{3*n*+1} nanosheets, with $n > 1$ (Figure 2b,e–g, Figure S3d–f, Supporting Information). For other Cs:Sn ratios than the ones mentioned above, no stable materials were obtained (Figure S11, Supporting Information), and we identified the presence of CsI in the resulting products.

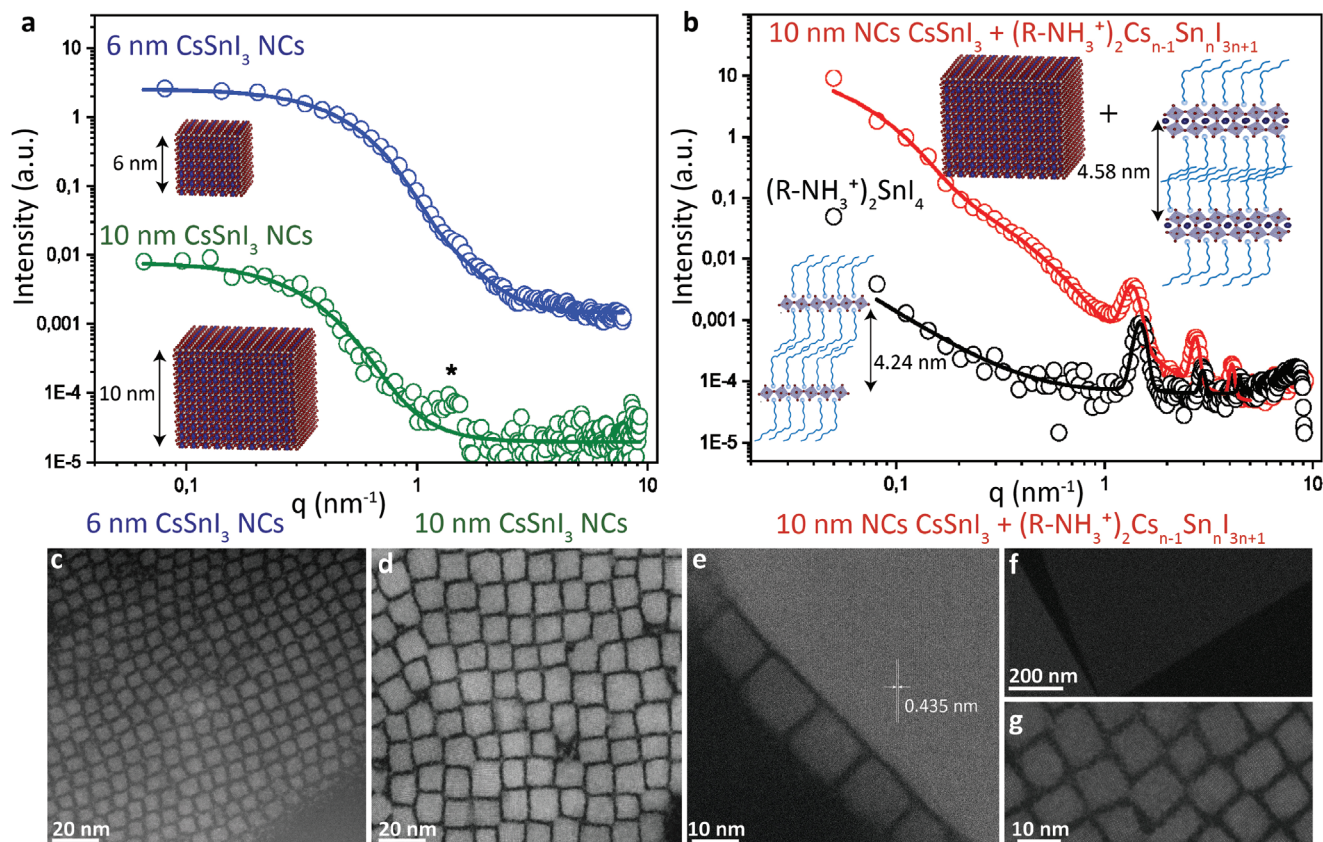


Figure 2. a) SAXS profiles for the $L_1 = 6$ nm (blue) and $L_1 = 10$ nm (green) $B-\gamma$ CsSnI₃ nanocrystals. Insets are schematic representations of the structures. b) SAXS profiles for the $L_1 = 10$ nm CsSnI₃ nanocrystals + (R-NH₃⁺)₂Cs_{*n*-1}Sn_{*n*}I_{3*n*+1} (red) compared with (R-NH₃⁺)₂SnI₄ control product. Insets are schematic representations of the structures. The continuous lines are fits of the data using opportune analytical geometrical models. c,d) STEM-HAADF images of $L_1 = 6$ and 10 nm $B-\gamma$ CsSnI₃ nanocrystals. e–g) STEM-HAADF images of $L_1 = 10$ nm CsSnI₃ nanocrystals + (R-NH₃⁺)₂Cs_{*n*-1}Sn_{*n*}I_{3*n*+1} with areas containing nanocuboids and nanosheets.

Our studies also revealed that temperature and reaction time do not affect the final product's composition, but only its colloidal stability (Figure S12, Supporting Information). On the other hand, the ligand ratios play a crucial role in the stability of the final NCs. We found that the Sn:OLA:OA ratios must be kept substoichiometric (Figure S13, Supporting Information) to prevent decomposition of the CsSnI₃ NCs over the course of time. The reason is that, if the Sn:ligands ratio is >2 with Cs:Sn = 1:3, when quenched with ice-water, the reaction reverts to a white turbid solution within minutes after reaching room temperature. This reaction mixture nucleates again at higher temperatures, and the process can be repeated for multiple cycles.

Next, we compared the structural dynamics between 3D CsSnI₃ NCs and 2D (R-NH₃⁺)₂Cs_{*n*-1}Sn_{*n*}I_{3*n*+1}. The formation of the CsSnI₃ with $L_1 = 6$ and 10 nm (Figure 2a,c,d) was confirmed by SAXS and STEM measurements. The presence of 2D (R-NH₃⁺)₂SnI₄ in the control reaction (Figure 2c), indicated that the growth of the 3D CsSnI₃ NCs starts from those Cs-free 2D structures. (R-NH₃⁺)₂SnI₄ perovskites have a 4.24 nm interlayer distance (Figure 2b, black plot, and Figure S10) in good agreement with the presence of long-chain oleylammonium cations. Depending on the Cs:Sn:ligands ratios, CsSnI₃ NCs or CsSnI₃ NCs together with (R-NH₃⁺)₂Cs_{*n*-1}Sn_{*n*}I_{3*n*+1}, $n > 1$ were synthesized as summarized below. For Cs:Sn = 1:3

we obtained stable and clean 3D CsSnI₃ perovskite NCs ($L_1 = 6$ and 10 nm) with minimal 2D components (Figure 2a). If the 2D perovskites were present in those cases (which depended on the washing procedure, see Sections S1.1 and S1.2, Supporting Information), they only formed as $n = 1$ (as shown by ssNMR, Figure S10b). For Cs:Sn = 1:2, 2D perovskites with nanosheet morphology were observed together with CsSnI₃ NCs with $L_1 = 10$ nm (Figure 2b,e,f). The distance between the inorganic layers was 4.58 nm, indicating more interconnected bent cis-oleylammonium chains than in (R-NH₃⁺)₂SnI₄. ssNMR showed an additional peak at -242.5 ppm in this case, while the peak corresponding to $n = 1$ was reduced in intensity (Figure S9a, Supporting Information). Note that we identified structural dynamics between (R-NH₃⁺)₂Cs_{*n*-1}Sn_{*n*}I_{3*n*+1} with $n = 1$ and $n > 1$ induced by spinning the sample during the ssNMR measurements, which indicated an overall instability of the 2D species under unusual conditions.

The confinement of the 2D perovskite with the structure (R-NH₃⁺)₂Cs_{*n*-1}Sn_{*n*}I_{3*n*+1} was analyzed using DFT by means of interlayer separation (d_{sep}) and octahedra layer stack screening. Layered models coming from a cubic phase, with no octahedral tilting, as well as tetragonal and orthorhombic phases, with octahedral tilting, were considered. Theoretical calculations at the HSE06 level (see the Supporting Information) indicate

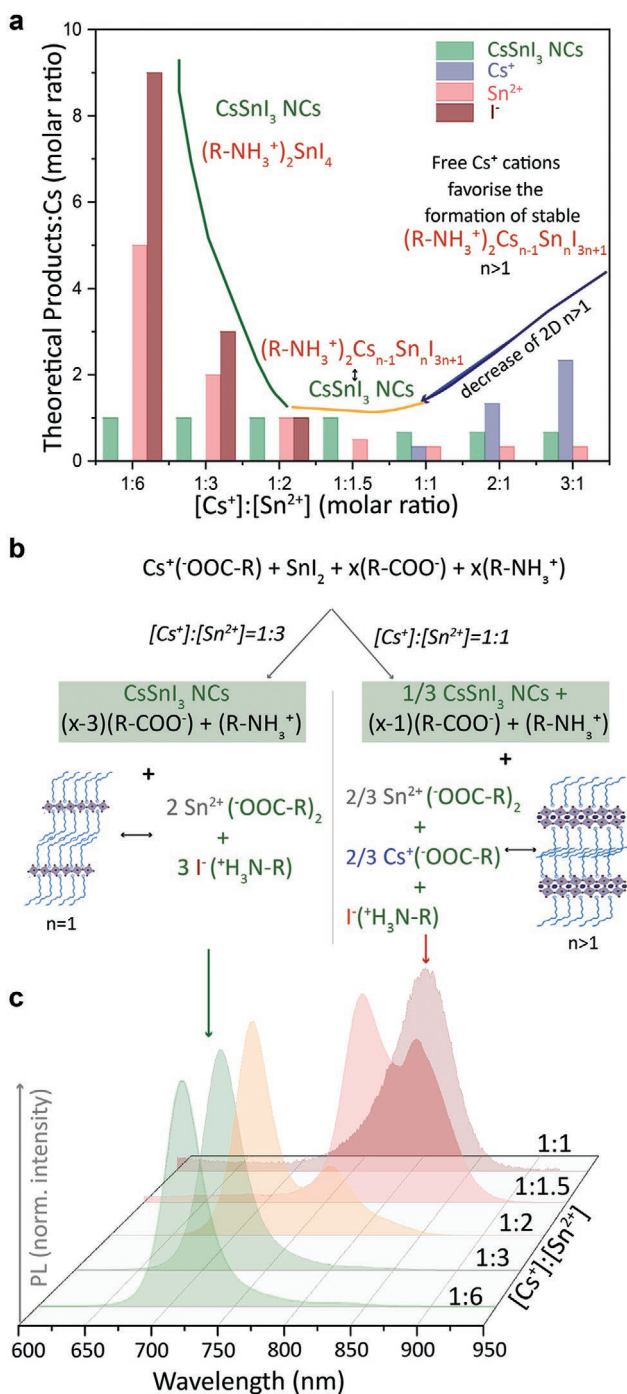


Figure 3. a) Representation of the theoretical ratio of final products versus Cs as a function of the Cs⁺:Sn²⁺ precursor ratio as calculated from the chemical reaction. b) Reaction scheme based on our experimental results for different ratios of Cs⁺:Sn²⁺. c) Experimental PL spectra and PL peak evolution for products obtained with different ratios of Cs⁺:Sn²⁺ precursors.

that the interlayer distance only negligibly affects the bandgap, suggesting that there is no significant impact on the electronic structure of the NC if the organic ligand length is varied, even when going to values as small as $d_{\text{sep}} = 15 \text{ \AA}$ (Figure S14, Supporting Information). The 2D sheet with γ -like tilting was

found to be the most stable structure (Table S2, Supporting Information), with a bandgap of 1.95 eV, in good accord with that registered experimentally and prior reports.^[22,31] Increasing the thickness of the sheet by incorporating additional layers of SnI₆⁴⁻ octahedra (n) leads to a progressive reduction of the bandgap: from 1.95 eV with $n = 1$ to 1.32 eV with $n = 4$ for 2D γ -CsSnI₃, thus approaching the bulk limit (Table S3, Figure S15, Supporting Information).

The optical properties of the CsSnI₃ NCs (Figure 4) with lateral sizes $L_1 = 6$ and 10 nm revealed PL peaks at 606 nm (2.05 eV, FWHM = 0.08 eV) and 714 nm (1.74 eV, FWHM = 0.1 eV), respectively, with PL quantum yields (PLQY) between 1% and 5%. The excitonic absorption peaks are well defined at 590 nm (2.1 eV) and 705 nm (1.76 eV), respectively, indicating a narrow size distribution of the NCs in each case. The samples containing NCs with $L_1 = 10$ nm and 2D (R-NH₃⁺)₂Cs_{n-1}Sn_nI_{3n+1} nanosheets with $n > 1$ showed a broader absorption feature (812 nm, 1.53 eV) and an emission peak at 825 nm, with FWHM = 0.08 eV (Figure 4a,b). For a proper comparison, we synthesized CsSnI₃ bulk powder following the method of Chung et al.,^[15] and obtained pure material with B- γ orthorhombic crystal structure, a ¹¹⁹Sn NMR peak at -152 ppm (Figure S16a,b, Supporting Information), and a bandgap of 1.25 eV (Figure S16c, Supporting Information).

DFT calculations predict an exponential decay of the bandgap upon increasing the NC size (Figure S6, Supporting Information) and asymptotic convergence to the bulk limit (≈ 1.3 eV). Since the extent of quantum size confinement depends on the exciton Bohr radius of the material, we applied the effective mass approximation (EMA)^[32] to calculate the effective diameter for the Wannier–Mott exciton (d_B) and the corresponding exciton binding energy (E_b) in CsSnI₃, and found $d_B = 4.4$ nm and $E_b = 73$ meV for γ -CsSnI₃ (see Section SIV and Table S4, Supporting Information). Similarly, small binding energies in the range of 20–80 meV have been reported in related lead halide perovskites.^[1,33] The confinement effect on the bandgap can then be estimated as in a spherical potential well of radius r according to $\Delta E_{\text{gap}} = \hbar^2 \pi^2 / (2\mu r^2)$, where μ is the reduced mass of the exciton. These bandgaps values correlate well with the experimental data (Figure S17, Supporting Information) and support the blue shift of the emission peak found in γ -CsSnI₃ for decreasing NC sizes (Figure 4b).

To track the photogenerated carriers in the Sn-based perovskite nanostructures, we performed time-resolved photoluminescence (TRPL) spectroscopy (Figure 4c). The lifetime decay was fitted with a bi-exponential function, indicating two decay channels. The pure NCs ($L_1 = 6$ and 10 nm) showed largely similar decay times with a significant contribution from the faster component, while for mixed $L_1 = 10$ nm and the 2D (R-NH₃⁺)₂Cs_{n-1}Sn_nI_{3n+1} nanosheets with $n > 1$, the slower component contributed more strongly (Table S5, Supporting Information). The inset of Figure 4c shows the evolution of the PL spectra at short delay times after the initial photoexcitation for the mixture of 3D NCs and 2D Sn perovskites nanosheets. The disappearance of the high energy tail in favor of a PL peak at 850 nm testifies to a fast energy transfer from the nanocrystals to the nanosheet.

The stability of the Sn-halide perovskite NCs was studied by analyzing their colloidal, chemical and optical behavior.

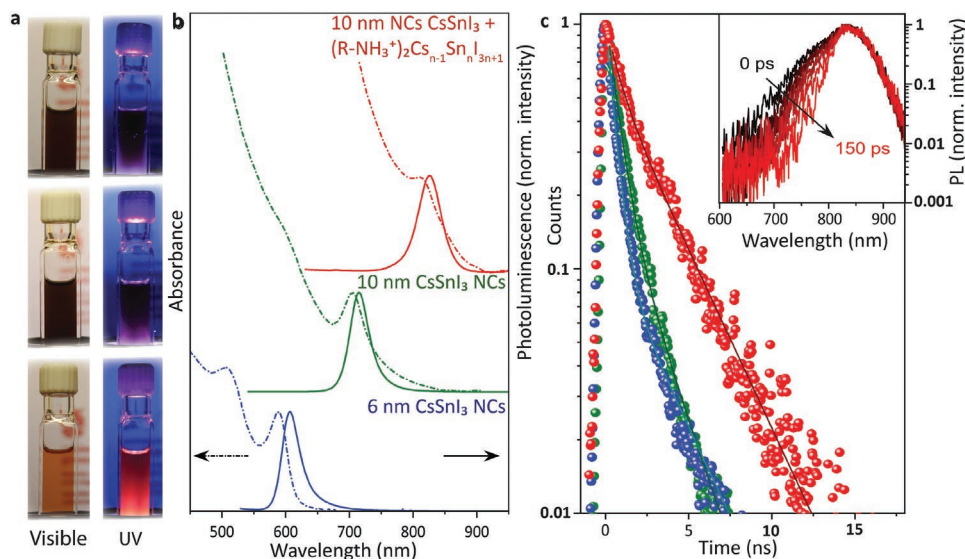


Figure 4. a) Photographs of cuvettes containing (bottom) $L_1 = 6$ nm B- γ -CsSnI₃ nanocrystals dispersed in hexane, (middle) $L_1 = 10$ nm B- γ -CsSnI₃ nanocrystals and (top) $L_1 = 10$ nm CsSnI₃ nanocrystals + (R-NH₃⁺)₂Cs_{*n*-1}Sn_{*n*13*n*+1}) nanosheets dispersed in toluene illuminated under visible and UV light (365 nm). b) Absorbance and PL spectra ($\lambda_{\text{exc}} = 500$ nm) and c) TRPL decay curve ($\lambda_{\text{exc}} = 400$ nm) of $L_1 = 6$ nm CsSnI₃ nanocrystals at $\lambda_{\text{em}} = 600$ nm (blue), $L_1 = 10$ nm B- γ -CsSnI₃ nanocrystals at $\lambda_{\text{em}} = 711$ nm (green), and $L_1 = 10$ nm CsSnI₃ nanocrystals + (R-NH₃⁺)₂Cs_{*n*-1}Sn_{*n*13*n*+1}) at $\lambda_{\text{em}} = 825$ nm (red). Inset: PL spectra of $L_1 = 10$ nm CsSnI₃ nanocrystals + (R-NH₃⁺)₂Cs_{*n*-1}Sn_{*n*13*n*+1}) nanosheets showing a high-energy tail decaying within 150 ps.

Successive dilution experiments showed that there is no significant blue- or redshift in absorbance (<2 nm) and PL (<6 nm); therefore, minimal aggregation-induced self-absorption is observed (Figure S18, Supporting Information). Moreover, this also indicates excellent colloidal stability in various concentrations; the preferred storage concentration was found to be 10 mg mL⁻¹. The optical and colloidal stability was preserved for NCs kept in an inert atmosphere for more than eight months as demonstrated by the optical measurements (Figure S19, Supporting Information) and STEM images (Figure S20, Supporting Information). In previous reports,^[9–11] the stability for similar NCs has been measured up to two months and the PLQY found to be below 1%. Drop-cast thin films prepared and studied in moisture and air free conditions showed good stability as seen from the absorbance measurements over time (Figure S21, Supporting Information). Even if the excitonic peak of the NCs is retained in the thin films for at least 15 days (Figure S21, Supporting Information), we noticed a relatively fast PL degradation (initial FWHM = 0.083 eV, after three days FWHM = 0.402 eV, pointing to localized merging of the cuboids due to the surface reconstruction and ligand removal. When CsSnI₃ NCs were exposed to air, their PL decayed in ≈ 1 h for solutions and 20 min for films. As expected, Cs₂SnI₆ was the main product in the decomposed materials (Figure S22, Supporting Information).

3. Conclusions

We have demonstrated that rational chemical design for synthesizing Sn halide perovskite nanostructures leads to stable CsSnI₃ NCs that are tunable in size, and optically active. Combining optical and structural characterization (STEM, ssNMR, SAXS, and XPS) with DFT computations, we were able to

identify the presence of 2D nanosheets RP perovskites with R-NH₃⁺. The synthetic routes toward fully inorganic 3D NCs or a mixture of 3D CsSnI₃ NCs and 2D RP perovskite nanosheets were demonstrated by varying the precursors ratios, highlighting the importance of the excess of SnI₂ compared to Cs⁺ in order to guide the system toward the desired final composition, structure and morphology. 2D (R-NH₃⁺)₂SnI₄ structures were identified as forming in the early growth stage of our explored syntheses. Importantly, substoichiometric ligands amounts are needed for the increased stability of the obtained NCs, and an excess of tin iodide complements this goal. The well-defined optical properties of the stable CsSnI₃ NCs with a lateral size of 10 nm, a bandgap of 1.76 eV and emission at 714 nm demonstrate the high potential of Sn halide perovskite NCs for opto-electronic applications. Efforts should now concentrate on understanding the surface chemistry and the carrier relaxation pathways to further increase the optical performance.

Supporting Information

Supporting Information is available from the Wiley Online Library or from the author.

Acknowledgements

This work was financially supported by the Dutch Research Council (NWO) via VENI grant number VI.Veni.192.048 and by the Advanced Materials research program of the Zernike National Research Centre under the Bonus Incentive Scheme of the Dutch Ministry for Education, Culture and Science. The X-ray scattering experiments were financed by the MEMOE grant number 17896 from NWO. The computational study was supported by the national and regional Spanish governments (PID2020-119748GA-I00 funded by MICIN/AEI/10.13039/501100011033, and APOSTD/2017/081). The authors acknowledge the technical support

from Arjan Kamp, Teo Zaharia, and Jacob Baas. The authors thank Jennifer Hong for the XRF measurements, and Kim van Adrichem and Diana Stancut for help with the materials synthesis. L.P. thanks Dr. Laura Piveteau for reading the manuscript.

Conflict of Interest

The authors declare no conflict of interest.

Data Availability Statement

The data that support the findings of this study are available from the corresponding author upon reasonable request.

Keywords

colloids, lead-free perovskites, nanocrystals, nanosheets, Ruddlesden-Popper perovskites, Sn-halide perovskites, synthesis mechanisms

Received: February 10, 2022

Revised: April 20, 2022

Published online:

- [1] L. Protesescu, S. Yakunin, M. I. Bodnarchuk, F. Krieg, R. Caputo, C. H. Hendon, R. X. Yang, A. Walsh, M. V. Kovalenko, *Nano Lett.* **2015**, *15*, 3692.
- [2] a) M. V. Kovalenko, L. Protesescu, M. I. Bodnarchuk, *Science* **2017**, *358*, 745; b) A. Dey, J. Ye, A. De, E. Debroye, S. K. Ha, E. Bladt, A. S. Kshirsagar, Z. Wang, J. Yin, Y. Wang, L. N. Quan, F. Yan, M. Gao, X. Li, J. Shamsi, T. Debnath, M. Cao, M. A. Scheel, S. Kumar, J. A. Steele, M. Gerhard, L. Chouhan, K. Xu, X.-g. Wu, Y. Li, Y. Zhang, A. Dutta, C. Han, I. Vincon, A. L. Rogach, et al., *ACS Nano* **2021**, *15*, 10775.
- [3] a) A. Kojima, K. Teshima, Y. Shirai, T. Miyasaka, *J. Am. Chem. Soc.* **2009**, *131*, 6050; b) A. K. Jena, A. Kulkarni, T. Miyasaka, *Chem. Rev.* **2019**, *119*, 3036.
- [4] a) S. D. Stranks, H. J. Snaith, *Nat. Nanotechnol.* **2015**, *10*, 391; b) X.-K. Liu, W. Xu, S. Bai, Y. Jin, J. Wang, R. H. Friend, F. Gao, *Nat. Mater.* **2021**, *20*, 10; c) J. Miao, F. Zhang, *J. Mater. Chem. C* **2019**, *7*, 1741.
- [5] L. Lei, Q. Dong, K. Gundogdu, F. So, *Adv. Funct. Mater.* **2021**, *31*, 2010144.
- [6] a) Gurudayal, D. S., M. H. Kumar, L. H. Wong, J. Barber, M. Grätzel, N. Mathews, *Nano Lett.* **2015**, *15*, 3833; b) J. Luo, J.-H. Im, T. Mayer, M. Schreier, K. Nazeeruddin Mohammad, N.-G. Park, S. D. Tilley, J. Fan Hong, M. Grätzel, *Science* **2014**, *345*, 1593.
- [7] A. Babayigit, H.-G. Boyen, B. Conings, *MRS Energy Sustainability* **2018**, *5*, E1.
- [8] P. Li, X. Liu, Y. Zhang, C. Liang, G. Chen, F. Li, M. Su, G. Xing, X. Tao, Y. Song, *Angew. Chem., Int. Ed.* **2020**, *59*, 6909.
- [9] a) T. C. Jellicoe, J. M. Richter, H. F. J. Glass, M. Tabachnyk, R. Brady, S. E. Dutton, A. Rao, R. H. Friend, D. Credgington, N. C. Greenham, M. L. Böhm, *J. Am. Chem. Soc.* **2016**, *138*, 2941; b) F. Liu, J. Jiang, T. Toyoda, M. A. Kamarudin, S. Hayase, R. Wang, S. Tao, Q. Shen, *ACS Appl. Nano Mater.* **2021**, *4*, 3958.
- [10] Q. Liu, J. Yin, B.-B. Zhang, J.-K. Chen, Y. Zhou, L.-M. Zhang, L.-M. Wang, Q. Zhao, J. Hou, J. Shu, B. Song, N. Shirahata, O. M. Bakr, O. F. Mohammed, H.-T. Sun, *J. Am. Chem. Soc.* **2021**, *143*, 5470.
- [11] C. Kang, H. Rao, Y. Fang, J. Zeng, Z. Pan, X. Zhong, *Angew. Chem., Int. Ed.* **2021**, *60*, 660.
- [12] a) B. Lyu, X. Guo, D. Gao, M. Kou, Y. Yu, J. Ma, S. Chen, H. Wang, Y. Zhang, X. Bao, *J. Hazard. Mater.* **2021**, *403*, 123967; b) Y. Wang, J. Tu, T. Li, C. Tao, X. Deng, Z. Li, *J. Mater. Chem. A* **2019**, *7*, 7683; c) L.-J. Chen, C.-R. Lee, Y.-J. Chuang, Z.-H. Wu, C. Chen, *J. Phys. Chem. Lett.* **2016**, *7*, 5028.
- [13] A. B. Wong, Y. Bekenstein, J. Kang, C. S. Kley, D. Kim, N. A. Gibson, D. Zhang, Y. Yu, S. R. Leone, L.-W. Wang, A. P. Alivisatos, P. Yang, *Nano Lett.* **2018**, *18*, 2060.
- [14] a) S. M. Wang, D. B. Mitzi, C. A. Feild, A. Guloy, *J. Am. Chem. Soc.* **1995**, *117*, 5297; b) D. B. Mitzi, *Chem. Mater.* **1996**, *8*, 791.
- [15] I. Chung, J.-H. Song, J. Im, J. Androulakis, C. D. Malliakas, H. Li, A. J. Freeman, J. T. Kenney, M. G. Kanatzidis, *J. Am. Chem. Soc.* **2012**, *134*, 8579.
- [16] C. C. Stoumpos, C. D. Malliakas, M. G. Kanatzidis, *Inorg. Chem.* **2013**, *52*, 9019.
- [17] K. Shum, Z. Chen, J. Qureshi, C. Yu, J. J. Wang, W. Pfenninger, N. Vockic, J. Midgley, J. T. Kenney, *Appl. Phys. Lett.* **2010**, *96*, 221903.
- [18] a) D. E. Scaife, P. F. Weller, W. G. Fisher, *J. Solid State Chem.* **1974**, *9*, 308; b) S. L. Suib, P. F. Weller, *J. Cryst. Growth* **1980**, *48*, 155.
- [19] a) J. Pascual, G. Nasti, M. H. Aldamasy, J. A. Smith, M. Flatken, N. Phung, D. Di Girolamo, S.-H. Turren-Cruz, M. Li, A. Dallmann, R. Avolio, A. Abate, *Mater. Adv.* **2020**, *1*, 1066; b) J. Pascual, M. Flatken, R. Félix, G. Li, S.-H. Turren-Cruz, M. H. Aldamasy, C. Hartmann, M. Li, D. Di Girolamo, G. Nasti, E. Hüsam, R. G. Wilks, A. Dallmann, M. Bär, A. Hoell, A. Abate, *Angew. Chem., Int. Ed.* **2021**, *60*, 21583.
- [20] C. Zhou, H. Lin, S. Lee, M. Chaaban, B. Ma, *Mater. Res. Lett.* **2018**, *6*, 552.
- [21] M. Chen, M.-G. Ju, M. Hu, Z. Dai, Y. Hu, Y. Rong, H. Han, X. C. Zeng, Y. Zhou, N. P. Padture, *ACS Energy Lett.* **2019**, *4*, 276.
- [22] D. H. Cao, C. C. Stoumpos, T. Yokoyama, J. L. Logsdon, T.-B. Song, O. K. Farha, M. R. Wasielewski, J. T. Hupp, M. G. Kanatzidis, *ACS Energy Lett.* **2017**, *2*, 982.
- [23] a) L. Ma, M.-G. Ju, J. Dai, X. C. Zeng, *Nanoscale* **2018**, *10*, 11314; b) M. C. Weidman, M. Seitz, S. D. Stranks, W. A. Tisdale, *ACS Nano* **2016**, *10*, 7830.
- [24] E. L. da Silva, J. M. Skelton, S. C. Parker, A. Walsh, *Phys. Rev. B* **2015**, *91*, 144107.
- [25] L.-M. Wang, J.-K. Chen, B.-B. Zhang, Q. Liu, Y. Zhou, J. Shu, Z. Wang, N. Shirahata, B. Song, O. F. Mohammed, O. M. Bakr, H.-T. Sun, *Nanoscale* **2021**, *13*, 16726.
- [26] Q. A. Akkerman, G. Rainò, M. V. Kovalenko, L. Manna, *Nat. Mater.* **2018**, *17*, 394.
- [27] R. G. Pearson, *J. Am. Chem. Soc.* **1963**, *85*, 3533.
- [28] a) H. Cox, A. J. Stace, *J. Am. Chem. Soc.* **2004**, *126*, 3939; b) O. Romiluyi, Y. Eatmon, R. Ni, B. P. Rand, P. Clancy, *J. Mater. Chem. A* **2021**, *9*, 13087; c) S. Zhang, P. Audebert, Y. Wei, A. Al Choueiry, G. Lanty, A. Bréhier, L. Galmiche, G. Clavier, C. Boissière, J.-S. Lauret, E. Deleporte, *Materials* **2010**, *3*, 3385; d) F. Hao, C. C. Stoumpos, P. Guo, N. Zhou, T. J. Marks, R. P. H. Chang, M. G. Kanatzidis, *J. Am. Chem. Soc.* **2015**, *137*, 11445.
- [29] M. Benavides-Garcia, K. Balasubramanian, *J. Chem. Phys.* **1994**, *100*, 2821.
- [30] a) K. Liang, D. B. Mitzi, M. T. Prikas, *Chem. Mater.* **1998**, *10*, 403; b) D. Di Girolamo, J. Pascual, M. H. Aldamasy, Z. Iqbal, G. Li, E. Radicchi, M. Li, S.-H. Turren-Cruz, G. Nasti, A. Dallmann, F. De Angelis, A. Abate, *ACS Energy Lett.* **2021**, *6*, 959.
- [31] a) Y. Liao, H. Liu, W. Zhou, D. Yang, Y. Shang, Z. Shi, B. Li, X. Jiang, L. Zhang, L. N. Quan, R. Quintero-Bermudez, B. R. Sutherland, Q. Mi, E. H. Sargent, Z. Ning, *J. Am. Chem. Soc.* **2017**, *139*, 8897; b) F. Li, Y. Xie, Y. Hu, M. Long, Y. Zhang, J. Xu, M. Qin, X. Lu, M. Liu, *ACS Energy Lett.* **2020**, *5*, 1422.

- [32] P. Y. Yu, M. Cardona, *Fundamentals of Semiconductors*, Springer, New York **1996**.
- [33] a) J. Even, L. Pedesseau, C. Katan, *J. Phys. Chem. C* **2014**, *118*, 11566; b) E. Menéndez-Proupin, P. Palacios, P. Wahnón, J. C. Conesa, *Phys. Rev. B* **2014**, *90*, 045207; c) J. M. Frost, K. T. Butler, F. Brivio, C. H. Hendon, M. van Schilfgaarde, A. Walsh, *Nano Lett.* **2014**, *14*, 2584; d) M. Saba, M. Cadelano, D. Marongiu, F. Chen, V. Sarritzu, N. Sestu, C. Figus, M. Aresti, R. Piras, A. Geddo Lehmann, C. Cannas, A. Musinu, F. Quochi, A. Mura, G. Bongiovanni, *Nat. Commun.* **2014**, *5*, 5049.